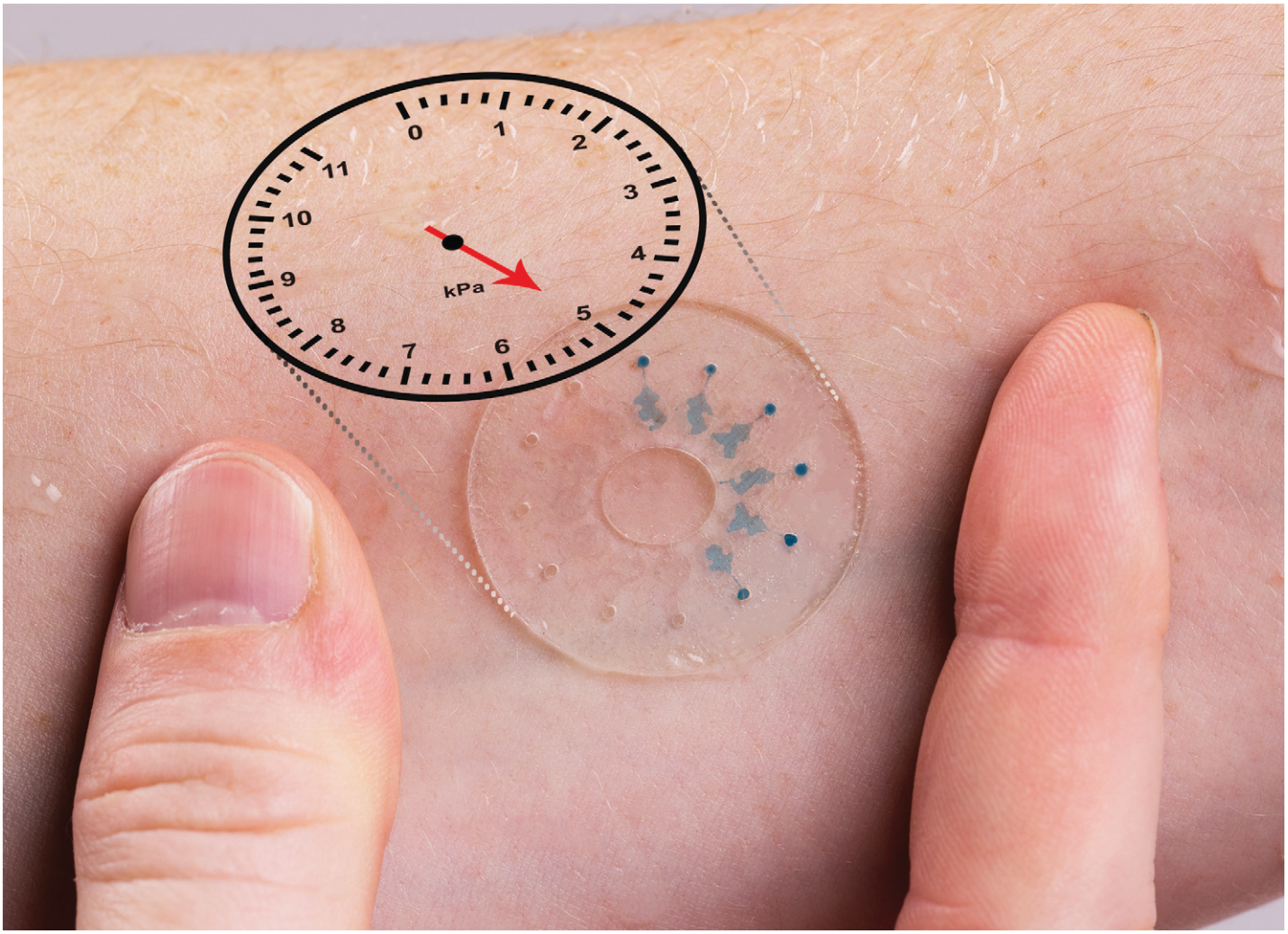

Featuring work from the Departments of Materials Science and Engineering, Dr. Jungil Choi and Prof. John A. Rogers, Northwestern University, United States.

Soft, skin-mounted microfluidic systems for measuring secretory fluidic pressures generated at the surface of the skin by eccrine sweat glands

We introduce a thin, soft wearable microfluidic system that mounts onto the surface of the skin to enable precise and routine measurements of secretory fluidic pressures generated at the surface of the skin by eccrine sweat glands.

As featured in:

See John A. Rogers *et al.*, *Lab Chip*, 2017, **17**, 2572.

ROYAL SOCIETY OF CHEMISTRY

rsc.li/loc

Registered charity number: 207890

Lab on a Chip

PAPER

View Article Online
View Journal | View Issue

Cite this: *Lab Chip*, 2017, **17**, 2572

Soft, skin-mounted microfluidic systems for measuring secretory fluidic pressures generated at the surface of the skin by eccrine sweat glands†

Jungil Choi, [a] Yeguang Xue, [b] Wei Xia, [c] Tyler R. Ray, [a] Jonathan T. Reeder, [a] Amay J. Bandodkar, [a] Daeshik Kang, [d] Shuai Xu, [e] Yonggang Huang [f] and John A. Rogers *[g]

Received 16th May 2017,
Accepted 16th June 2017

DOI: 10.1039/c7lc00525c

rsc.li/loc

During periods of activity, sweat glands produce pressures associated with osmotic effects to drive liquid to the surface of the skin. The magnitudes of these pressures may provide insights into physiological health, the intensity of physical exertion, psychological stress factors and/other information of interest, yet they are currently unknown due to absence of means for non-invasive measurement. This paper introduces a thin, soft wearable microfluidic system that mounts onto the surface of the skin to enable precise and routine measurements of secretory fluidic pressures generated at the surface of the skin by eccrine sweat glands (surface SPSG, or s-SPSG) at nearly any location on the body. These platforms incorporate an arrayed collection of unit cells each of which includes an opening to the skin, an inlet through which sweat can flow, a capillary bursting valve (CBV) with a unique bursting pressure (BP), a corresponding microreservoir to receive sweat and an outlet to the surrounding ambient to allow release of backpressure. The BPs systematically span the physiologically relevant range, to enable a measurement precision approximately defined by the ratio of the range to the number of unit cells. Human studies demonstrate measurements of s-SPSG under different conditions, from various regions of the body. Average values in healthy young adults lie between 2.4 and 2.9 kPa. Sweat associated with vigorous exercise have s-SPSGs that are somewhat higher than those associated with sedentary activity. For all conditions, the forearm and lower back tend to yield the highest and lowest s-SPSGs, respectively.

Introduction

Emerging capabilities in thin, soft skin-mounted electronic technologies enable precise continuous monitoring of many clinical parameters related to physiological status.[1,2] The associated potential for improvements in human healthcare are significant, beyond anything that can be realistically envisioned with conventional rigid devices that couple to the wrist or the chest with bands or straps. Many classes of skin-like, or 'epidermal', electronic systems are now available in research labs and early commercial forms, including clinical-quality sensors for electrocardiography,[3] electromyography,[4] temperature,[5] blood flow,[6] blood oximetry,[7] hydration[8] and many others.[9–12] Recent work qualitatively extends the capabilities of such skin-interfaced platforms through the addition of soft, 'epidermal' microfluidic systems that can capture, store and chemically analyze sweat naturally released from the surface of the skin.[13–16] These devices, with or without electronic functionality, softly seal to the skin in a manner that allows sweat glands to pump sweat into microfluidic networks where various measurements can be performed. Demonstrations include sweat rate, total sweat

[a] *Departments of Materials Science and Engineering, Northwestern University, Evanston, IL 60208, USA*
[b] *Department of Civil and Environmental Engineering, Mechanical Engineering, and Materials Science and Engineering, Northwestern University, Evanston, IL 60208, USA*
[c] *State Key Laboratory for Strength and Vibration of Mechanical Structures, Xi'an Jiaotong University, Xi'an, Shaanxi 710049, China*
[d] *Department of Mechanical Engineering, Ajou University, San 5, Woncheon-Dong, Yeongtong-Gu, Suwon 16499, Korea*
[e] *Department of Dermatology, Feinberg School of Medicine, Northwestern University, Chicago, IL 60611, USA*
[f] *Center for Bio-Integrated Electronics, Department of Civil and Environmental Engineering, Mechanical Engineering, and Materials Science and Engineering, Northwestern University, Evanston, IL 60208, USA*
[g] *Center for Bio-Integrated Electronics, Departments of Materials Science and Engineering, Biomedical Engineering, Chemistry, Mechanical Engineering, Electrical Engineering and Computer Science, and Neurological Surgery, Simpson Querrey Institute for Nano/biotechnology, McCormick School of Engineering and Feinberg School of Medicine, Northwestern University, Evanston, IL 60208, USA. E-mail: jrogers@northwestern.edu*

† Electronic supplementary information (ESI) available. See DOI: 10.1039/c7lc00525c

loss and pH, along with the concentration of glucose, lactate, chloride and creatinine.[17–19] Advanced designs allow time sequential sampling and storage of sweat for purposes of capturing temporal changes in sweat chemistry.[14] Alternative advanced technologies for continuous sweat analytics use absorbent pads or gels, without microfluidic structures, primarily for electrochemical analysis. Possibilities range from concentrations of metabolites such as glucose,[11,20–22] lactate,[23] and alcohol[24] to electrolytes such as sodium,[25,26] chloride,[27] calcium,[28] to various heavy metal ions.[29] Glucose in sweat is proportional to blood glucose, with the potential to serve as a biomarker for diabetes;[30,31] lactate is related to sweat generation rate and is a function of metabolic activity;[32–34] chloride concentration is a diagnostic for cystic fibrosis[35] and it provides important insights into overall electrolyte balance; heavy metal ions can yield an early indication of exposure to toxic metals. Although significant research activity focuses on measurement of these and other chemical species, the physical characteristics associated with the underlying processes of sweating have not been studied due to lack of suitable metrology methods.

Sweat glands operate by osmotic pressures produced by differences in osmolality between plasma and sweat.[34] Specifically, the concentrations of sodium and chloride in sweat are higher than those in the plasma, thereby producing pressure that induces flow of sweat from the glands through ducts that terminate at the skin surface. Using conventional techniques, the secretory pressure of the sweat glands (SPSG) can be difficult or impossible to determine under natural conditions. In 1969, Schulz *et al.* used an external, lab-scale manometer connected to a micropipette inserted into the sweat duct to measure the SPSG at this location on immobilized human subjects during sweating induced by introduction of pilocarpine into the skin by iontophoresis.[36] The mean values of pressures determined in this manner are ~40 kPa, with a remarkably broad range, from ~3 to ~70 kPa. Although simple engineering models of flow through the microfluidic structures of the glands and ducts suggest that such pressures are reasonable based on observed sweat rates,[34] additional examples of experimental studies cannot be found in the literature, likely due to difficulties associated with the measurements. The development of convenient approaches to determine s-SPSG in real-time, during normal activities across a range of body locations could rekindle interest in the physical metrology of sweating, where pressure, combined with cumulative and instantaneous flow rates, could provide interesting insights into exercise physiology.

The following introduces a thin, soft, skin-mounted microfluidic device for measuring the SPSG at the surface of the skin (s-SPSG) from small, well-defined collections of sweat glands. The device uses an arrayed collection of microfluidic structures, each with a capillary bursting valve (CBV) selected with a different bursting pressure (BP) across a physiologically relevant range. Here, each CBV passes liquid only if the pressure of the flow exceeds that of the BP, as defined by its engineered geometry. In an array of CBVs, each with a slightly different BP, the largest/smallest BPs that are smaller/larger than the s-SPSG define the pressure to within an uncertainty determined by the difference between these two BPs. A simple platform based on this concept yields capabilities that allow, to our knowledge, the first measurements of s-SPSG associated with naturally occurring sweat under realistic scenarios. Studies based on human subjects and different parts of the body under various conditions provide an initial set of data on the physiological and physical aspects of sweat generation and flow.

Results and discussion

Thin, soft microfluidic devices for measuring secretory fluidic pressures generated at the surface of the skin by eccrine sweat glands

The devices consist of three layers of soft, elastomeric materials: a uniform capping layer, a microfluidic layer with microchannels, microreservoirs, CBVs, inlets (to the skin) and outlets (to the surrounding ambient) and an adhesive layer with openings to the skin that align with the inlets (Fig. 1a–d). The devices adhere to the skin to a degree that does not allow lateral propagation of sweat or other forms of leakage, up to s-SPSG values of ~15 kPa (Fig. S1†). Conformal contact of the adhesive layer effectively prevents any significant lateral flow of sweat from regions away from the defined openings.[15] When a sweat pore is blocked by the device, it is reabsorbed into the sweat duct. Each inlet connects to a microfluidic channel that leads to a CBV (Fig. 1c) as an entry point to a corresponding microreservoir. An outlet at the opposite side of the microreservoir eliminates backpressure would otherwise result from trapped air. If the s-SPSG is higher than the BP, then flow occurs and the microreservoir fills with sweat. If the s-SPSG is lower than the BP, then flow does not occur and the microreservoir does not fill with sweat (Fig. 1e and f). Evaluation of filling patterns across an array of such structures with CBVs that have BPs distributed throughout a physiologically relevant range allows for direct assessment of the s-SPSG.

Fabrication details are in the method section and Fig. S2.† Bonding between the channel and capping layer occurs by completing the curing process (10 min at 70 °C in an oven) with the two layers in contact.[37] The contact angle of water on PDMS processed in this manner is 120.6° ± 0.5° (Fig. S3†). This parameter is critical in the design of CBVs. The three circular posts in each chamber prevent collapse.

Arrays of CBVs for measuring sweat pressure

In vitro experiments determine the BPs of CBVs with a range of channel widths between 20 μm to 100 μm (Fig. S4a and b†), thereby establishing the relationship between width and BP (Fig. S4b†). Pilot tests with various such platforms on the skin of healthy young volunteers define a relatively narrow range of s-SPSG values, *i.e.* from 2.1 to 2.3 kPa (Fig. S4c and d†), for use with subjects in the studies described subsequently. The final device designs include 12 CBVs, each with a different BP, with widths from 10 μm to 120 μm at increments of 10 μm (Fig. 2a). Each CBV leads to a separate

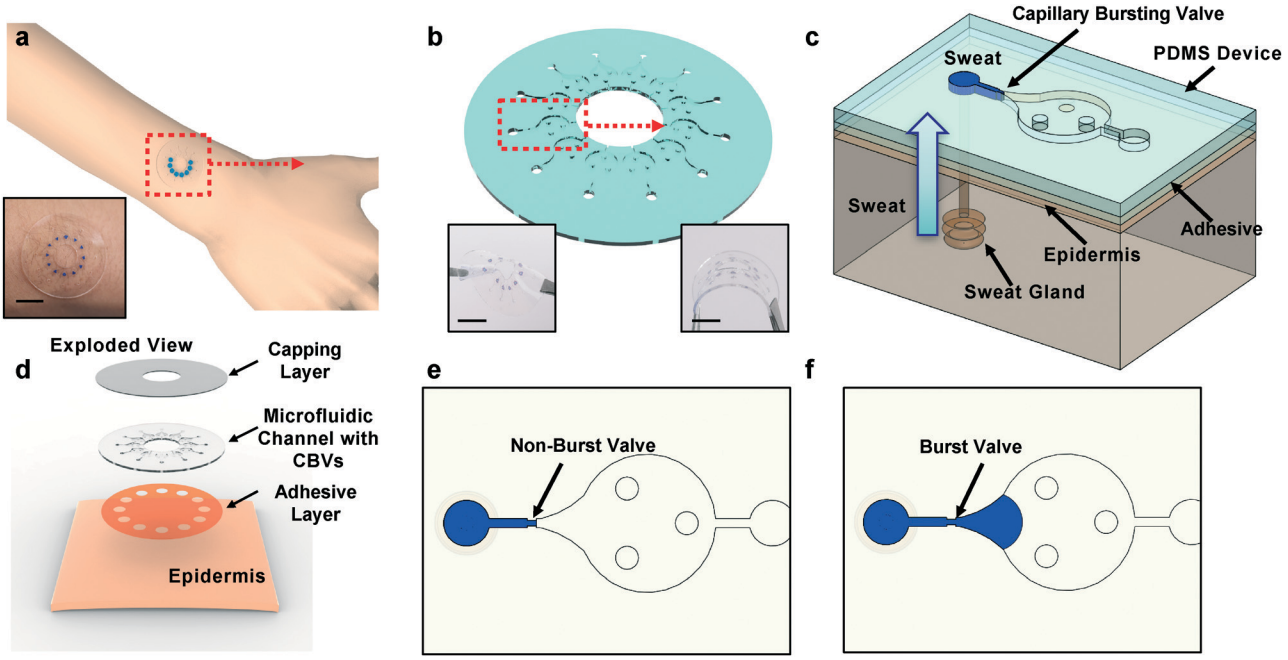

Fig. 1 a) Schematic illustrations and optical images (inset) of soft, skin-mounted microfluidic systems for measuring the secretory pressure from sweat glands, at the surface of the skin. Inset: Photograph of a device on the skin b) perspective view illustration of a device with 12 capillary bursting valves. Insets: Optical images of device a twisted (left) and bent (right) state. c) Perspective view illustration of a single capillary bursting valve integrated onto the skin, with a representative sweat gland. d) Exploded view illustration of a device and its interface with the skin. Top view illustrations of microfluidic channels partially filled with blue-dyed water for cases of a e) valve that is not yet burst and f) a valve that has burst. Scale bar represents 10 mm in a and b.

microreservoir and corresponding inlet, adhesive opening and outlet. As example, images in Fig. 2b show CBV #1, #5 and #9, which have widths 120, 80 and 40 μm, respectively. For human testing, a colorimetric indicator of sweat inserted into each microreservoir allows rapid visual readout (Fig. 2c). As an example of operation, if the sweat pressure is sufficiently high to burst CBV #5 and but not #6, then microreservoirs #1–#5 fill, and change in color from blue to pink, but #6–#12 remain empty (Fig. 2d and e, S5a and b†). The s-SPSG of the skin is determined as the highest BP among the burst CBVs, *i.e.* #5 in this example. The volume of the channel that leads to the CBV is only 0.1 μl (Fig. S5c†). Even

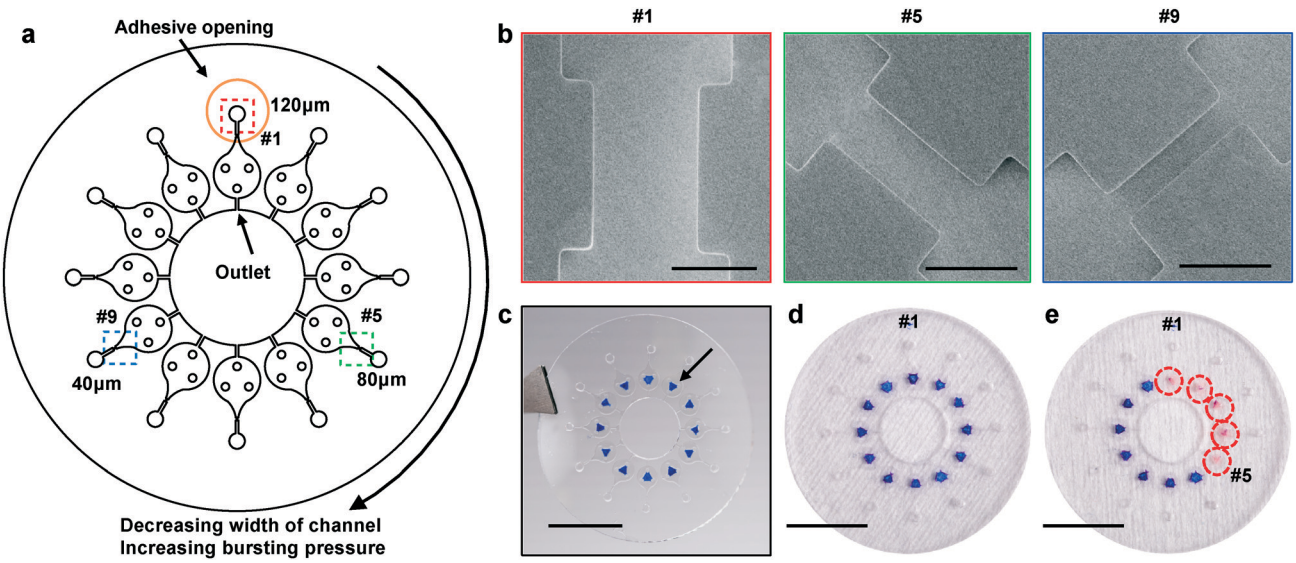

Fig. 2 a) Top view illustration of microfluidic channels with 12 different CBVs, each designed with a different BP by control of the width of the channel. b) Scanning electron microscope images of the CBVs #1, #5 and #9. c) Optical image of a device with cobalt chloride ($CoCl_2$) in 2% pHEMA at the center of each chamber. Optical image of a device d) before bursting of the CBVs and e) after bursting of CBVs #1–#5. Scale bars represent 100 μm in b and 10 mm in c and e.

modest rates of sweating fill this volume quickly. If the flow of sweat stops at the valve, the surface area of the sweat open to the chamber is only 0.01 mm^2. As a result, the amount of sweat available to generate vapor is extremely small. The total volume of the chamber is ~0.8 μl. Previous studies indicate that the sweat rate from the skin under the device for typical conditions is approximately 0.6 μl per min per gland. When the s-SPSG is higher than the BP, the sweat quickly fills the chamber. No observable condensation occurred in any of the chambers during the time of testing.

Experimental measurement and mechanics modeling of BPs

The Young–Laplace equation describes the BP for a rectangular channel as[38,39]

$$\mathrm{BP} = -2\sigma\left[\frac{\cos\theta_1^*}{b} + \frac{\cos\theta_A}{h}\right], \quad (1)$$

where σ is surface tension of liquid, θ_A is the critical advancing contact angle of the channel, θ_1^* is the $\min[\theta_A + \beta, 180°]$, β is diverging angle of the channel, b and h are the width and height of the diverging section, respectively. The surface tension of sweat and, therefore, the BPs can be affected by the presence of oils and other substances from the skin, as well as temperature. All reported tests involved preparation of the skin by use of an alcohol wipe immediately before mounting the devices, as a means to eliminate oils and other contaminants. The skin temperature in all cases was within a range from 30 to 37 °C, typical of exercise.[40] The estimated temperature related changes in BP are, therefore, within 3% of the nominal value, and can be neglected.

Analysis of scanning electron microscope images allows accurate determination of the channel dimensions (Table S1†). The critical advancing contact angle follows from measuring the angle at the moment when a drop just starts to move across the surface of a tilted PDMS slab.[41] The advancing contact angle of water on PDMS is 125° ± 2°, which is slightly larger than the stationary contact angle, 120.6° (Fig. S3c†).

Imperfections in the fabrication process lead to slight rounding of the edges at the exit regions of the CBVs, thereby increasing the effective width of the channel (Fig. 3b). For CBVs with rounded edges, the position of advancing interface marked by θ_e ($0 \le \theta_e \le \beta$, Fig. S6a†) is undetermined, and the bursting pressure given by eqn (1) becomes

$$\mathrm{BP} = -2\sigma\left[\frac{\cos\theta_1^*}{b_e} + \frac{\cos\theta_A}{h}\right], \quad (2)$$

where $b_e = b + 2r_e(1 - \cos\theta_e)$, r_e is radius of rounding edge, and $\theta_1^* = \min\{\theta_A + \theta_e, \pi\}$. The bursting pressure BP varies as

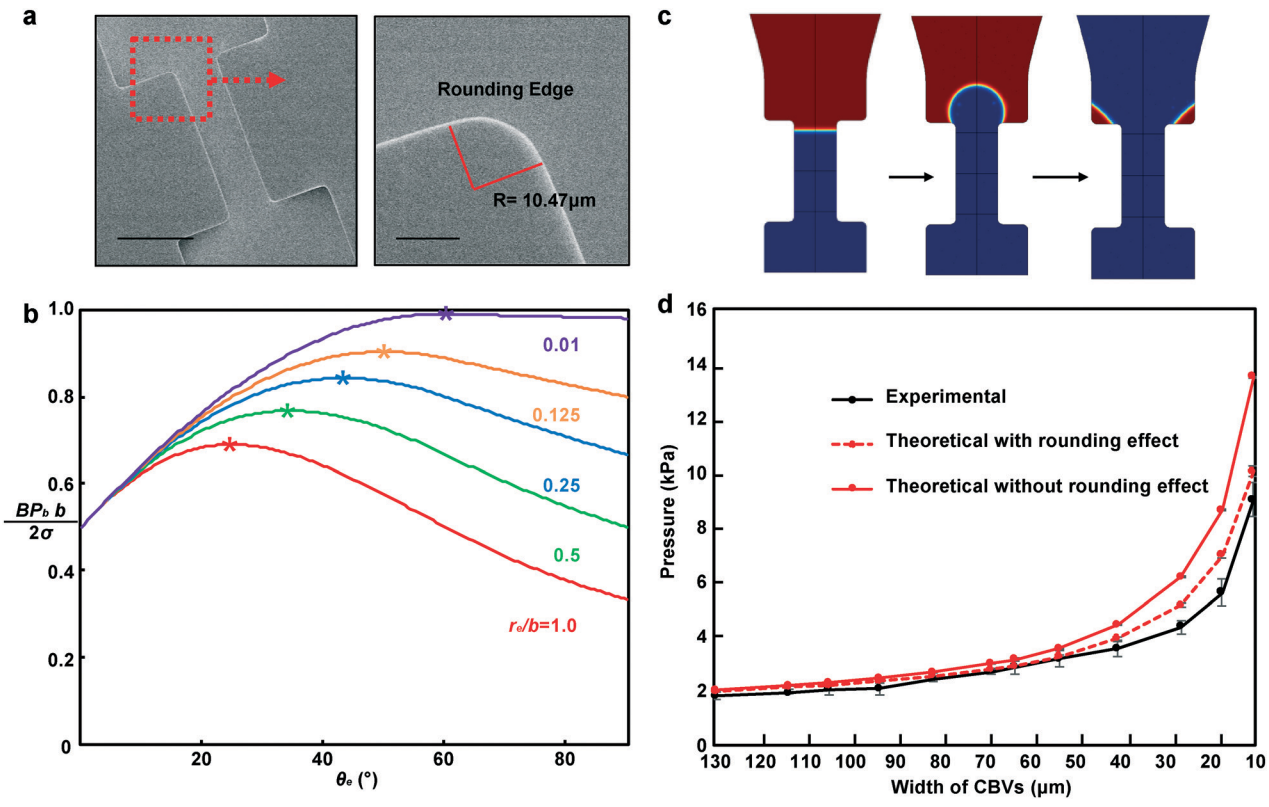

Fig. 3 Experimental measurements and numerical calculations of bursting pressures of CBVs. a) Scanning electron microscope images of the edges of representative CBVs. b) Calculated values of the bursting pressure term from wall according to the θ_e. c) Images from numerical simulations of flow past a bursting valve. d) Bursting pressure of CBVs from experimental tests and theoretical calculations with and without the effects of rounding. Scale bars represents 100 μm in the upper image in a.

the advancing interface moves, and the final critical bursting pressure BP_{cr} is determined by maximizing eqn (2) with respect to the advancing interface position θ_e. Because the second term of eqn (2) (defined as $BP_h = -2\sigma\frac{\cos\theta_A}{h}$) is independent of θ_e, we focus on the first term (defined as $BP_b = -2\sigma\frac{\cos\theta_f^*}{b_e}$. For $\beta > \pi - \theta_A$ (as in real application), BP_b can be written as

$$\frac{BP_b b}{2\sigma} = \frac{-\cos(\theta_A + \theta_e)}{1 + 2(r_e/b)(1-\cos\theta_e)}, \quad 0 \le \theta_e \le \pi - \theta_A \tag{3}$$

$$\frac{BP_b b}{2\sigma} = \frac{-1}{1 + 2(r_e/b)(1-\cos\theta_e)}, \quad \pi - \theta_A \le \theta_e \le \beta \tag{4}$$

Fig. 3b shows $\frac{BP_b b}{2\sigma}$ versus θ_e for $\beta = 90°$, $\theta_A = 120°$ and r_e/b = 0.01, 0.125, 0.25, 0.5, 1.0. The peak points marked by stars correspond to the critical $(BP_b)_{cr}$ determined by maximizing BP_b with respect to interface position θ_e. It is also shown that the critical bursting pressure decreases with increasing rounding radius r_e/b, and the model degenerates to Young–Laplace equation when $r_e/b = 0$. The analytical solution is verified with 2D numerical simulations (Fig. 3c and S5b†) and the predicted BPs for different CBV widths show better consistency with the measured values *in vitro* tests compared to the model that does not consider the rounded edges (Fig. 3d and S7†).

Uncertainties in measuring s-SPSGs

Uncertainties in the measured s-SPSGs involve contributions from slight variations in the critical dimensions of the CBVs and from spatial heterogeneity in the characteristics of sweat glands across the skin. Concerning the first, *in vitro* tests reveal that percentage variations in the BPs for nominally identical CBVs lie in the range of ~10% (Table S1†). The second contribution arises from a device architecture that uses 12 separate inlets, each of which captures sweat from a different region of the skin. In tests involving 25 min of cycling exercise, devices with identical CBVs for all inlets (Fig. S8a†) show bursting in 10 (out of 12), 11 (out of 12) and 1 (out of 12) CBVs with BPs of 1.7, 1.9 and 2.0 kPa, respectively (Fig. S8b†). In this case, 1.9 kPa corresponds to the s-SPSG of the region. The device with separate CBVs at 1.7, 1.9, 2.0 kPa and higher BP will yield a s-SPSG of 1.9 with 84% probability. The effect of different behaviors of individual sweat glands and variations in their density contribute in a minor way to uncertainties in the s-SPSG determined from regions with statistically meaningful numbers of glands.

This type of uncertainty can be avoided with a device design that includes a single inlet (Fig. S9†) and a single, interconnected microfluidic structure. Here, the first CBV has the lowest bursting pressure and largest width. The BP increases monotonically, by virtue of decreasing widths, in a clockwise direction around an interconnected array. The sweat fills the system up to the CBV that has a BP larger than the s-SPSG. For certain applications, this design might provide an attractive alternative to the system in Fig. 1. The disadvantage is that sweat flow from a single region must be sufficient to fill the device up to the point of a CBV that does not burst. All *in situ* measurements of s-SPSG used the device design with separate inlets.

In situ measurement of the s-SPSG in various human subject studies

Human testing involved evaluations on healthy young adult volunteers during exercise with three different types of fitness equipment (stationary bikes, elliptical trainers and treadmills) and in at-rest sessions in a sauna room. The studies included devices mounted on the forearm, upper arm, chest, upper back, lower back and thigh (Fig. 4a), with pressure measurements after 20 min in each scenario. The pressures correspond, then, to the maximum values during this interval. The inlet areas are each 7 mm^2. Since the densities of sweat glands at the forearm, upper arm, chest, upper back, lower back and thigh are 108, 102, 91, 106, 132 and 102 glands per cm^2, respectively,[42] the number of sweat glands per inlet is 7–9. Experiments with devices that have inlets with diameters of 2, 3 and 4 mm, in both exercising on an elliptical machine and sitting in a sauna room, show comparable s-SPSGs (Fig. S10†). Additional control experiments to examine the effects of compensatory sweating that arise from blockage of sweat glands by the adhesive involved devices that have diameters of 30, 40 and 50 mm mounted on forearm, upper arm and chest, as summarized in Fig. S11a.† Although the 40 mm case yielded the highest SPSG and the 50 mm yielded the lowest (Fig. S11b†), the variations are small and statistically insignificant; they likely arise from biological variabilities in sweat gland physiology and density.

From the fundamental physics of pressure-driven fluid flow, the pressure differential from the end of the duct to the outside air is proportional to sweat flow rate.[43] Studies confirm the secretory pressure of sweat glands tends to increase with sweat rate.[36] Our measurements of s-SPSGs and sweat rate at the forearm is consistent with such behavior, although the data exhibit some scatter (Fig. S12†).

During cycling, the s-SPSG is lowest at the upper arm and lower back (1.8 ± 0.1 kPa) and highest at the thigh (3.2 ± 0.3 kPa). During elliptical exercise, the s-SPSG is lowest at the lower back (1.8 ± 0.1 kPa) and highest at the forearm (5.6 ± 0.5 kPa). Averaged from six positions across the body, the elliptical exercise and the sauna produce the highest (from 5.6 ± 0.5 to 1.8 ± 0.1 kPa) and lowest (from 3.2 ± 0.3 to 1.8 ± 0.1 kPa) pressures (Fig. 4c). As an attempt to explain these differences, consider that the pressure generated at the location of a sweat gland is given by

$$P = \sigma RT\Delta C \tag{5}$$

where σ is the osmotic reflection coefficient, R is the ideal gas constant, T is the temperature of the body, and ΔC is the

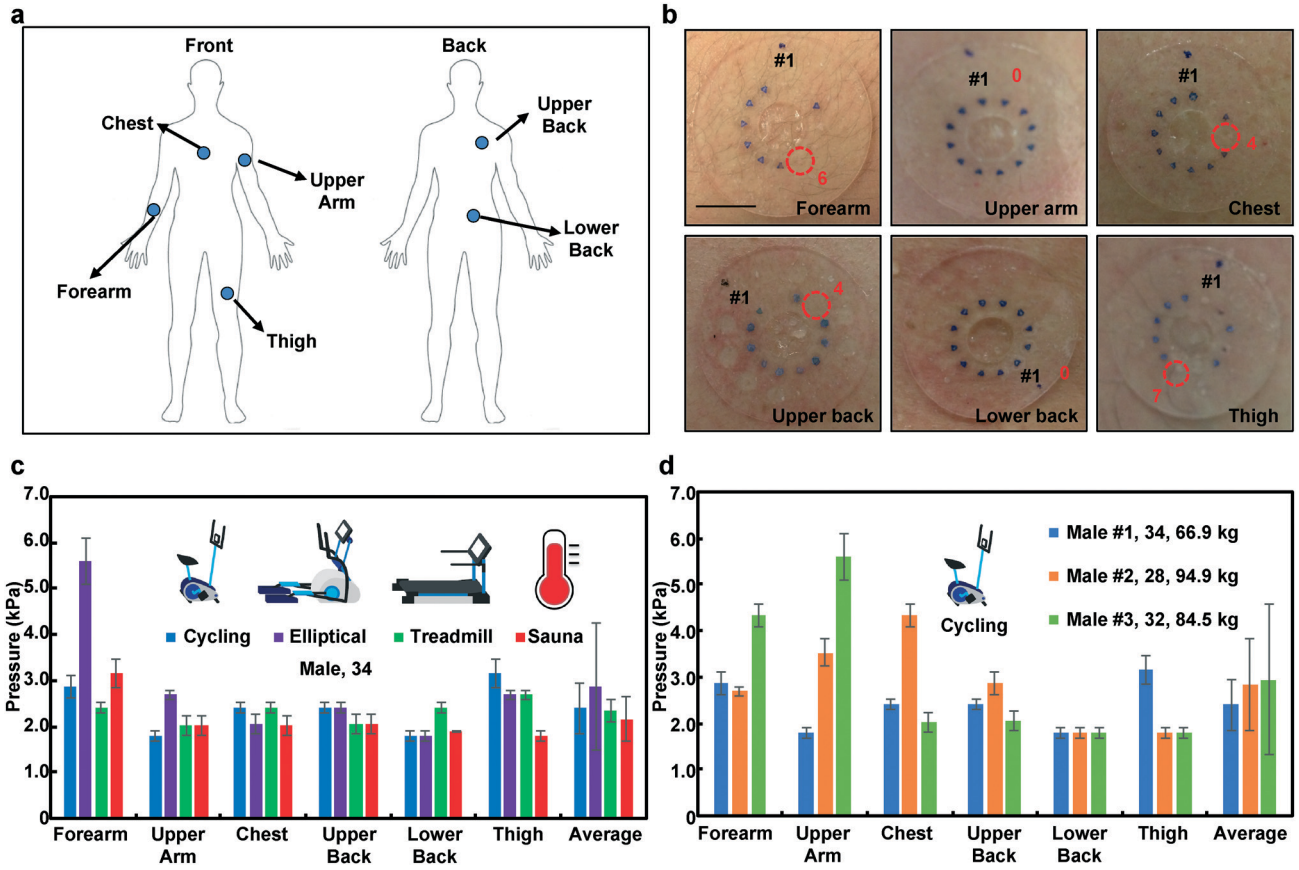

Fig. 4 *In situ* measurements of s-SPSG from various body positions during different exercising routines and thermal exposure. a) Mounting positions on the body; forearm, upper arm, chest, upper back, lower back and thigh, b) optical images of the measurement of s-SPSG from cycling exercise from various positions on the body. Measured pressures c) from different conditions (cycling, exercising at elliptical, treadmill and thermal exposure) and regions of the body from a 34 year old male volunteer d) from three different volunteers during cycling exercise. Scale bar represents 10 mm in b.

difference in concentration between sweat and plasma, which defines the osmolality.[34] The measured concentrations of chloride in sweat generated by cycling and sitting in a sauna are 65 ± 2 and 66 ± 2 mM, respectively. These values are identical, within experimental uncertainties, and therefore cannot account for the observed differences in pressure. Another possibility is that physical movement of the muscles and surrounding tissues, and other physiological processes such as vasodilation associated with vigorous exercise, can increase the s-SPSG. Measurements using devices placed on the forehead and behind the ear, where motion effects are minimal, show s-SPSG values lower than those on other regions of the body (Fig. S13†). The acceleration from the movement of body could, conceivably, affect the behavior of the CBVs and therefore measured pressure.[44–46] Control experiments performed with devices mounted on PDMS substrates that moved rapidly and deformed by stretching and compressing, while applying constant fluid pressure to the CBVs (Fig. S14†), show an absence of motion related effects on the operation of the CBVs. The small volume of sweat in the inlet channels (0.1 μl) helps to minimize such inertial effects (Fig. S5c†).

The overall SPSGs lie between 1.8 ± 0.1 and 5.6 ± 0.5 kPa. These values are smaller than those (41.4 ± 18.6 kPa) reported previously in tests that require introduction of a micropipette into the sweat duct while artificially stimulating sweat with a chemical inducing agent (pilocarpine). These differences are likely due to the combined effects of pressure drops along the duct and differences between natural and induced sweating.

From cycling tests, all three subjects produced the highest s-SPSG at the thigh and upper arm (3.2 ± 0.3 kPa), at the chest and lower back (4.3 ± 0.3 kPa) and at the upper arm and lower back (5.6 ± 0.5 kPa). One subject produced the lowest s-SPSG at the lower back (1.8 ± 0.1 kPa) and two others at the thigh (1.8 ± 0.1 kPa) (Fig. 4d). The wide range suggests that this parameter might have utility in studies of exercise physiology. For example, muscles produce 90% of the metabolic heat during exercise[47] and increases in body temperature trigger vasodilation and sweating.[48] Because the sweat pressure follows from interactions between sweat and plasma in blood, variations in body temperature and blood flow might contribute to differences in s-SPSG.[49,50] These effects, and those related to age (*i.e.* the oldest subject produced the smallest range (1.8 ± 0.1–3.2 ± 0.3 kPa) from six positions across the body and the lowest average s-SPSG (2.4 ± 0.5 kPa)), might be interesting to explore in future work.

Conclusions

In summary, the results presented here show that arrays of capillary bursting valves in epidermal microfluidic devices can serve as platforms for convenient, routine measurements of secretory fluidic pressures generated at the surface of the skin by eccrine sweat glands. These systems can be non-invasively applied to nearly any region of the body, without irritation or discomfort or constraint in activity. Systematic experimental and theoretical studies establish a basis for quantitatively using these devices in a range of scenarios. Investigations with volunteer subjects illustrate measurement capabilities in a variety of sweating conditions, across different body locations and individuals. These measurements, particularly when coupled with analysis of key biomarkers in sweat, provide many opportunities for future studies of sweat physiology.

Methods

Device fabrication

Spin coating KMPR 1010 (Microchem, MA, United States) at 3000 rpm for 30 s formed a 15 μm thick layer of photoresist on a silicon wafer. After photolithography and development, deep reactive ion etching (STS Pegasus ICP-DRIE, SPTS Technologies Ltd) created trenches to a depth of 90 μm on the surface of the wafer. Next, spin coating formed a thin layer of PMMA (Microchem, MA, United States) on the mold to facilitate release of the cured PDMS. Pouring a prepolymer to PDMS (10 : 1 base : curing agent, Sylgard 184, Dow corning, MI, United States) on the mold, spin coating at 200 rpm and partially curing (70 °C oven for 15 min) formed the channel layer (thickness ~400 μm). Color change associated with water contact of a solution of 100 mg mL^{-1} cobalt(II) chloride ($CoCl_2$) dissolved in 2% polyhydroxyethylmethacrylate (pHEMA, wt%) hydrogel (Sigma-Aldrich, MO, United States) introduced into each of the microreservoirs by pipetting facilitated visualization of their filling with sweat (Fig. S5a†). Small volumes, *i.e.* 0.3 μl, of sweat changed the color of the indicator from blue to pink, sufficient for easy observation by eye (Fig. S5b†). A similar spin casting and partial curing process, but at 400 rpm on a bare wafer, yielded the capping layer (thickness ~200 μm). A 1 mm diameter circular punch formed holes at the inlets of the channel layer. A 8 mm diameter circular punch defined a hole through the channel and capping layers at the center of the device. Completing the curing process with the capping and channel layers in contact bonded the aligned pre-cured capping layer and fully-cured microfluidic channel layer. Corona treatment of the bottom surface of the device allowed bonding of an adhesive layer with a 3 mm diameter circular hole at the center (PC2723U, Scapa Healthcare). The openings for the inlets have diameters of 1 mm.

In vitro measurement of bursting pressure

A microfluidic control system (Fluigent MFCS, Villejuif, France) generated flows of artificial sweat for *in vitro* measurements of BPs. The artificial sweat consisted of an aqueous solution of 22×10^{-3} M of urea, 2.2×10^{-3} M of glucose, 3.8×10^{-3} M of potassium, 31×10^{-3} M of sodium, 58×10^{-3} M of chloride, and 5.2×10^{-3} M of calcium (Sigma-Aldrich, MO, USA). The microfluidic control system supplied pressure to the liquid using an air pump and while measuring the pressure of the liquid (Fig. S5†). After setting a desired pressure using the microfluidic control system, and maintaining this pressure for ~10 s, observation by eye identified the threshold for bursting of the valve.

In situ measurement of secretory pressure from human trials

Testing involved healthy young adults as volunteers during normal physical activity with no additional human-subject risk. All subjects provided their consent prior to participation. Rubbing with an alcohol wipe prepared the skin to ensure robust adhesion to the device. The exercising routine included cycling, elliptical and treadmill machines for 20 min at an approximate constant working load at room temperature (20 °C). The thermal exposures involved sitting at rest in a dry sauna at 50 °C for 20 min. For measuring sweat rate, we used a hydrophilic foam dressing and evaluated the weight of foam before and after exercise.

In vitro measurement of chloride concentration

A colorimetric chloride assay kit defined the chloride concentration (Sigma-Aldrich, MO, United States). The chrono-sampling device introduced in a previous study captured sweat during exercising and thermal exposure.[14] Dilution of 3 μl of sweat with 27 μl deionized water produced samples for analysis. Mixing 3 μl of sample with 27 μl of solution from the assay kit allowed colorimetric analysis based on spectroscopic measurements (NanoDrop) of the absorbance at a wavelength of 620 nm. Prepared solutions of 25, 50, 75, 100 and 125 mM sodium chloride served to set the standard curve for determining chloride concentration.

Contact angle measurement

A contact angle goniometer (VCA-Optima XE, MA, United States of America) yielded static contact angles and critical advancing angles of de-ionized water on PDMS. An automated dispenser yielded 1 μl droplets for these measurements.

Image acquisition

A scanning electron microscope (SEM, S-4800-II, Hitachi, Tokyo, Japan) and a digital microscope (VHX-5000, KEYENCE, Osaka, Japan) produced micrographs of the devices.

Acknowledgements

This work utilized Northwestern University Micro/Nano Fabrication Facility (NUFAB), which is partially supported by Soft and Hybrid Nanotechnology Experimental (SHyNE) Resource

(NSF NNCI-1542205), the Materials Research Science and Engineering Center (NSF DMR-1121262), the State of Illinois, and Northwestern University. Y. X. gratefully acknowledges support from the Ryan Fellowship and the Northwestern University International Institute for Nanotechnology. Y. H. acknowledges the support from NSF (Grant No. CMMI-1400169 and CMMI-1534120) and the NIH (Grant No. R01EB019337). We thank the Center for Bio-Integrated Electronics for support of this work. This work was supported by the Ajou University research fund.

References

1 S. Patel, H. Park, P. Bonato, L. Chan and M. Rodgers, *J. Neuroeng. Rehabil.*, 2012, **9**, 21.
2 A. Pantelopoulos and N. G. Bourbakis, *IEEE Trans. Syst., Man, Cybern. C, Appl. Rev.*, 2010, **40**, 1–12.
3 S. Xu, Y. Zhang, L. Jia, K. E. Mathewson, K. I. Jang, J. Kim, H. Fu, X. Huang, P. Chava, R. Wang, S. Bhole, L. Wang, Y. J. Na, Y. Guan, M. Flavin, Z. Han, Y. Huang and J. A. Rogers, *Science*, 2014, **344**, 70–74.
4 W. H. Yeo, Y. S. Kim, J. Lee, A. Ameen, L. Shi, M. Li, S. Wang, R. Ma, S. H. Jin, Z. Kang, Y. Huang and J. A. Rogers, *Adv. Mater.*, 2013, **25**, 2773–2778.
5 L. Gao, Y. Zhang, V. Malyarchuk, L. Jia, K. I. Jang, R. C. Webb, H. Fu, Y. Shi, G. Zhou, L. Shi, D. Shah, X. Huang, B. Xu, C. Yu, Y. Huang and J. A. Rogers, *Nat. Commun.*, 2014, **5**, 4938.
6 R. C. Webb, A. P. Bonifas, A. Behnaz, Y. H. Zhang, K. J. Yu, H. Y. Cheng, M. X. Shi, Z. G. Bian, Z. J. Liu, Y. S. Kim, W. H. Yeo, J. S. Park, J. Z. Song, Y. H. Li, Y. G. Huang, A. M. Gorbach and J. A. Rogers, *Nat. Mater.*, 2013, **12**, 1078.
7 J. Kim, P. Gutruf, A. M. Chiarelli, S. Y. Heo, K. Cho, Z. Q. Xie, A. Banks, S. Han, K. I. Jang, J. W. Lee, K. T. Lee, X. Feng, Y. G. Huang, M. Fabiani, G. Gratton, U. Paik and J. A. Rogers, *Adv. Funct. Mater.*, 2017, **27**, 1604373.
8 X. Huang, Y. H. Liu, H. Y. Cheng, W. J. Shin, J. A. Fan, Z. J. Liu, C. J. Lu, G. W. Kong, K. Chen, D. Patnaik, S. H. Lee, S. Hage-Ali, Y. G. Huang and J. A. Rogers, *Adv. Funct. Mater.*, 2014, **24**, 3846–3854.
9 D. J. Lipomi, M. Vosgueritchian, B. C. Tee, S. L. Hellstrom, J. A. Lee, C. H. Fox and Z. Bao, *Nat. Nanotechnol.*, 2011, **6**, 788–792.
10 A. Chortos and Z. N. Bao, *Mater. Today*, 2014, **17**, 321–331.
11 H. Lee, T. K. Choi, Y. B. Lee, H. R. Cho, R. Ghaffari, L. Wang, H. J. Choi, T. D. Chung, N. Lu, T. Hyeon, S. H. Choi and D. H. Kim, *Nat. Nanotechnol.*, 2016, **11**, 566–572.
12 S. Lee, A. Reuveny, J. Reeder, S. Lee, H. Jin, Q. Liu, T. Yokota, T. Sekitani, T. Isoyama, Y. Abe, Z. Suo and T. Someya, *Nat. Nanotechnol.*, 2016, **11**, 472–478.
13 J. C. Yeo, Kenry and C. T. Lim, *Lab Chip*, 2016, **16**, 4082–4090.
14 J. Choi, D. Kang, S. Han, S. B. Kim and J. A. Rogers, *Adv. Healthcare Mater.*, 2017, **6**, 1601355.
15 A. Koh, D. Kang, Y. Xue, S. Lee, R. M. Pielak, J. Kim, T. Hwang, S. Min, A. Banks, P. Bastien, M. C. Manco, L. Wang, K. R. Ammann, K. I. Jang, P. Won, S. Han, R. Ghaffari, U. Paik, M. J. Slepian, G. Balooch, Y. Huang and J. A. Rogers, *Sci. Transl. Med.*, 2016, **8**, 366ra165.
16 J. Heikenfeld, *Electroanalysis*, 2016, **28**, 1242–1249.
17 Y. H. Yang, S. Y. Xing, Z. C. Fang, R. Y. Li, H. Koo and T. R. Pan, *Lab Chip*, 2017, **17**, 926–935.
18 G. Matzeu, C. Fay, A. Vaillant, S. Coyle and D. Diamond, *IEEE Trans. Biomed. Eng.*, 2016, **63**, 1672–1680.
19 S. Coyle, D. Morris, K.-T. Lau, D. Diamond, N. Taccini, D. Costanzo, P. Salvo, F. Di Francesco, M. G. Trivella and J.-A. Porchet, *Pervasive Computing Technologies for Healthcare*, 2009.
20 H. Lee, C. Song, Y. S. Hong, M. S. Kim, H. R. Cho, T. Kang, K. Shin, S. H. Choi, T. Hyeon and D. H. Kim, *Sci. Adv.*, 2017, **3**, e1601314.
21 A. J. Bandodkar, W. Z. Jia, C. Yardimci, X. Wang, J. Ramirez and J. Wang, *Anal. Chem.*, 2015, **87**, 394–398.
22 W. Gao, S. Emaminejad, H. Y. Nyein, S. Challa, K. Chen, A. Peck, H. M. Fahad, H. Ota, H. Shiraki, D. Kiriya, D. H. Lien, G. A. Brooks, R. W. Davis and A. Javey, *Nature*, 2016, **529**, 509–514.
23 S. Imani, A. J. Bandodkar, A. M. Mohan, R. Kumar, S. Yu, J. Wang and P. P. Mercier, *Nat. Commun.*, 2016, **7**, 11650.
24 J. Kim, I. Jeerapan, S. Imani, T. N. Cho, A. Bandodkar, S. Cinti, P. P. Mercier and J. Wang, *ACS Sens.*, 2016, **1**, 1011–1019.
25 A. J. Bandodkar, D. Molinnus, O. Mirza, T. Guinovart, J. R. Windmiller, G. Valdes-Ramirez, F. J. Andrade, M. J. Schoning and J. Wang, *Biosens. Bioelectron.*, 2014, **54**, 603–609.
26 D. P. Rose, M. E. Ratterman, D. K. Griffin, L. L. Hou, N. Kelley-Loughnane, R. R. Naik, J. A. Hagen, I. Papautsky and J. C. Heikenfeld, *IEEE Trans. Biomed. Eng.*, 2015, **62**, 1457–1465.
27 A. Koh, D. Kang, Y. Xue, S. Lee, R. M. Pielak, J. Kim, T. Hwang, S. Min, A. Banks, P. Bastien, M. C. Manco, L. Wang, K. R. Ammann, K. I. Jang, P. Won, S. Han, R. Ghaffari, U. Paik, M. J. Slepian, G. Balooch, Y. G. Huang and J. A. Rogers, *Sci. Transl. Med.*, 2016, **8**, 366ra165.
28 H. Y. Nyein, W. Gao, Z. Shahpar, S. Emaminejad, S. Challa, K. Chen, H. M. Fahad, L. C. Tai, H. Ota, R. W. Davis and A. Javey, *ACS Nano*, 2016, **10**, 7216–7224.
29 W. Gao, H. Y. Y. Nyein, Z. Shahpar, H. M. Fahad, K. Chen, S. Emaminejad, Y. J. Gao, L. C. Tai, H. Ota, E. Wu, J. Bullock, Y. P. Zeng, D. H. Lien and A. Javey, *ACS Sens.*, 2016, **1**, 866–874.
30 J. Moyer, D. Wilson, I. Finkelshtein, B. Wong and R. Potts, *Diabetes Technol. Ther.*, 2012, **14**, 398–402.
31 K. Sakaguchi, Y. Hirota, N. Hashimoto, W. Ogawa, T. Hamaguchi, T. Matsuo, J.-I. Miyagawa, M. Namba, T. Sato and S. Okada, *J. Diabetes Sci. Technol.*, 2013, **7**, 678–688.
32 M. J. Buono, N. V. L. Lee and P. W. Miller, *J. Physiol. Sci.*, 2010, **60**, 103–107.
33 S. Biagi, S. Ghimenti, M. Onor and E. Bramanti, *Biomed. Chromatogr.*, 2012, **26**, 1408–1415.
34 Z. Sonner, E. Wilder, J. Heikenfeld, G. Kasting, F. Beyette, D. Swaile, F. Sherman, J. Joyce, J. Hagen, N. Kelley-Loughnane and R. Naik, *Biomicrofluidics*, 2015, **9**, 031301.

35 P. M. Farrell, B. J. Rosenstein, T. B. White, F. J. Accurso, C. Castellani, G. R. Cutting, P. R. Durie, V. A. LeGrys, J. Massie, R. B. Parad, M. J. Rock and P. W. Campbell, *J. Pediatr.*, 2008, **153**, S4–S14.
36 I. J. Schulz, *J. Clin. Invest.*, 1969, **48**, 1470–1477.
37 M. A. Eddings, M. A. Johnson and B. K. Gale, *J. Micromech. Microeng.*, 2008, **18**, 067001.
38 H. Cho, H. Y. Kim, J. Y. Kang and T. S. Kim, *J. Colloid Interface Sci.*, 2007, **306**, 379–385.
39 C. P. Huang, J. Lu, H. Seon, A. P. Lee, L. A. Flanagan, H. Y. Kim, A. J. Putnam and N. L. Jeon, *Lab Chip*, 2009, **9**, 1740–1748.
40 S. F. Fonseca, M. C. Teles, V. G. C. Ribeiro, F. C. Magalhaes, V. A. Mendonca, M. F. D. Peixoto, L. H. R. Leite, C. C. Coimbra and A. C. R. Lacerda, *Braz. J. Med. Biol. Res.*, 2015, **48**, 1122–1129.
41 Y. Yuan and T. R. Lee, in *Surface science techniques*, Springer, 2013, pp. 3–34.
42 N. A. Taylor and C. A. Machado-Moreira, *Extrem. Physiol. Med.*, 2013, **2**, 4.
43 L. L. Hou, J. Hagen, X. Wang, I. Papautsky, R. Naik, N. Kelley-Loughnane and J. Heikenfeld, *Lab Chip*, 2013, **13**, 1868–1875.
44 K. Yoo, U. Park and J. Kim, *Sens. Actuators, A*, 2011, **166**, 234–240.
45 J. C. Kuo, P. H. Kuo, Y. T. Lai, C. W. Ma, S. S. Lu and Y. J. J. Yang, *J. Microelectromech. Syst.*, 2013, **22**, 646–654.
46 C. Y. Huang, P. Sun, M. S. Lee, S. Y. Wu, Y. C. Shieh and W. Y. Hsu, *IEEE Sens. J.*, 2016, **16**, 654–661.
47 C. B. Wenger, *Exercise and Core Temperature*, Military Performance, Division US Army Research Institute of Environmental Medicine Natick, 1999.
48 N. Charkoudian, *Mayo Clin. Proc.*, 2003, **78**, 603–612.
49 D. J. Casa, S. M. Becker, M. S. Ganio, C. M. Brown, S. W. Yeargin, M. W. Roti, J. Siegler, J. A. Blowers, N. R. Glaviano, R. A. Huggins, L. E. Armstrong and C. M. Maresh, *J. Athl. Train.*, 2007, **42**, 333–342.
50 N. Kondo, S. Takano, K. Aoki, M. Shibasaki, H. Tominaga and Y. Inoue, *Acta Physiol. Scand.*, 1998, **164**, 71–78.

